Journal Pre-proof

Investigation of structural, microstructural and magnetic properties of $Yb_xY_{1-x}F_3$ solid solutions

Jelena Aleksić, Tanja Barudžija, Dragana Jugović, Miodrag Mitrić, Marko Bošković, Zvonko Jagličić, Darja Lisjak, Ljiljana Kostić

Please cite this article as: J. Aleksić, T. Barudžija, D. Jugović, M. Mitrić, M. Bošković, Z. Jagličić, D. Lisjak, L. Kostić, Investigation of structural, microstructural and magnetic properties of $Yb_xY_{1-x}F_3$ solid solutions, *Journal of Physics and Chemistry of Solids* (2020), doi: https://doi.org/10.1016/j.jpcs.2020.109449.
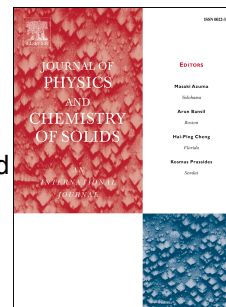
CRediT author statement

Jelena Aleksić: Conceptualizations, Formal analysis, Writing - Original Draft,

Tanja Barudžija: Writing - Review & Editing,

Dragana Jugović: Visualization, Investigation

Miodrag Mitrić: Methodology, Validation

Marko Bošković: Investigation

Zvonko Jagličić: Investigation

Darja Lisjak: Investigation

Ljiljana Kostić: Supervision

Investigation of structural, microstructural and magnetic properties of $Yb_xY_{1-x}F_3$ solid solutions

Jelena Aleksić [a], Tanja Barudžija [b,1], Dragana Jugović [c], Miodrag Mitrić [b], Marko Bošković [b], Zvonko Jagličić [d], Darja Lisjak [e], Ljiljana Kostić [a]

[a] Faculty of Sciences and Mathematics, University of Niš, Višegradska 33, 18000 Niš, Serbia

[b] Institute of Nuclear Sciences "Vinča", University of Belgrade, P.O. Box 522, 11001 Belgrade, Serbia

[c] Institute of Technical Sciences of SASA, Knez Mihailova 35/IV, 11000 Belgrade, Serbia

[d] Institute of Mathematics, Physics and Mechanics & University of Ljubljana, Faculty of Civil and Geodetic Engineering, Jadranska 19, SI-1000 Ljubljana, Slovenia

[e] Jožef Stefan Institute, Jamova 39, SI-1000 Ljubljana, Slovenia

Abstract

In this investigation, we have synthesized $Yb_xY_{1-x}F_3$ solid solutions by fluorination of yttrium and ytterbium sesquioxides with ammonium hydrogen difluoride. According to the XRD analysis, all synthesized $Yb_xY_{1-x}F_3$ samples have an orthorhombic crystal structure belonging to the β-YF_3 structural type. The refinement of crystal structure was done by the Rietveld method within the *Pnma* space group using the TCH pseudo-Voigt function. The anisotropic peak broadening was analyzed, and the average apparent crystallite size is about 50 nm with a small anisotropy of shape, while the significant microstrain that is highly anisotropic is present in all samples. The temperature-dependent magnetic susceptibility was analyzed by applying the model of a free ion perturbed by the crystal field. We have obtained the effective magnetic quantum numbers M_{ieff} of four Kramer's doublets of Yb^{3+} ion along with the entire crystal field splitting of the $^2F_{7/2}$ manifold of Yb^{3+} in YF_3. The acquired maximum energy splitting of the ground level is about 150 K in our most diluted samples. The field-dependent isothermal magnetization measurements were carried out at various temperatures and analyzed by classical Langevin function. Results obtained from magnetic measurements show that all $Yb_xY_{1-x}F_3$ ($x \neq 0$) solid solutions exibit pure paramagnetic behavior in the whole temperature range from 2 to 300 K, with a predominant antiferromagnetic exchange interactions.

[1] Corresponding author.
E-mail address: tbarudzija@vinca.rs (T. Barudžija).

1. Introduction

Rare-earth inorganic materials have received significant research attention during the past because of their specific electronic, magnetic, optical, and chemical properties that arise from partially occupied $4f$ electronic shells [1–13]. Recently, they have become more popular thanks to the advancement of synthesis of nanostructured materials and morphology-controlled synthesis [14–21]. These materials have a decisive role in areas such as optoelectronic devices, biomedical imaging, solid-state lasers, and scintillators [22–31]. Among many inorganic materials, yttrium trifluoride (YF_3), pure and doped with rare-earth ions ($RE_xY_{1-x}F_3$, RE = Tb^{3+}, Tm^{3+}, Eu^{3+}, Yb^{3+}, Er^{3+}, Dy^{3+}, Ce^{3+}, Pr^{3+}, and Ho^{3+}), has been thoroughly investigated as a promising host crystal for lanthanide-doped phosphor materials with interesting up/down conversion luminescent properties [32–36].

Yttrium trifluoride and trifluorides of the lanthanide elements from samarium to lutetium crystallize in orthorhombic β-YF_3 structure type in space group *Pnma* (No. 62), with four molecules in a unit cell. In this structure, cations occupy $4c$ Wyckoff position (x, ¼, z), and the fluorine ions occupy $4c$ (x, ¼, z) and $8d$ general positions (x, y, z) [37]. The three-dimensional structure consists of irregular nine-coordination YF_9 polyhedra linked over mutual corners, edges, and faces. Around every polyhedron, there are eleven adjacent polyhedra. Every polyhedron shares the face with the two nearest polyhedra, the edge with the other two polyhedra, and the corner with the seven remaining adjacent polyhedra. Face-sharing polyhedra build chains aligned with the *a*-axis (Fig. 1), and every chain is related laterally with six neighboring chains by mutual edges and corners.

The β-YF_3 structure of YF_3 and REF_3 (RE = Er, Tm, Yb, and Lu) is not stable in the whole temperature region up to the melting point [38,39]. As the temperature rises, a structural phase transition from orthogonal *Pnma* to a trigonal $P\bar{3}m1$ symmetry occurs, which is known as an α-YF_3 structure. The appropriate transition temperatures are 1267 K and 1350 K for YbF_3 and YF_3, respectively [40]. The transition temperature of $Yb_xY_{1-x}F_3$ solid solutions, which are the topic of this work, is somewhere between these two temperatures, and it decreases with the increasing concentration of the ytterbium ions [41]. In the temperature range of concern in this paper, the obtained solid solutions exist in structure type β-YF_3.
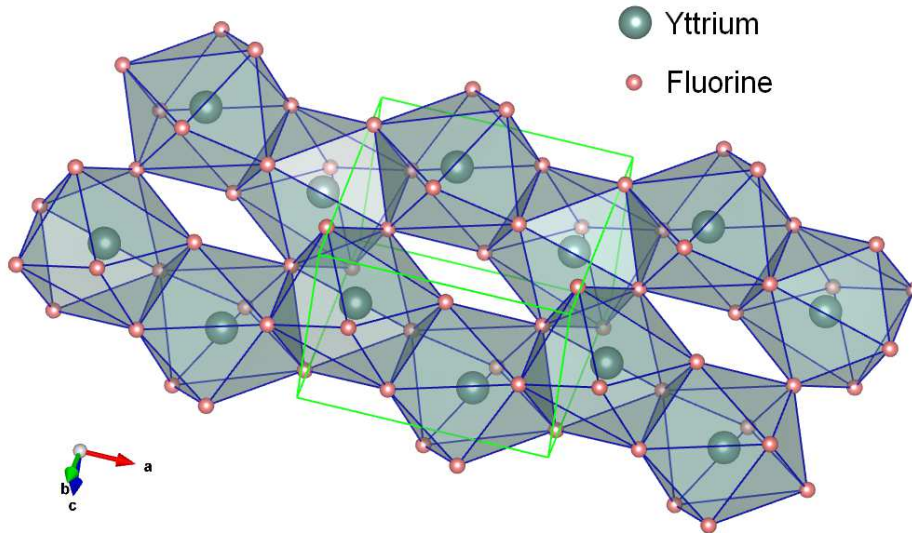
Fig. 1. The orthorhombic crystal structure of β-YF$_3$.

Owing to the similar ionic radius of Y^{3+} to lanthanides, trivalent rare-earth ions can easily replace the yttrium ions in orthorhombic YF$_3$ without additional charge compensation. YF$_3$ represents a suitable candidate for a host material, due to its high ionicity and coordination number, which results in a wide band gap (> 10 eV) and low vibrational energies [42]. Rare-earth trifluorides also show a diversity of magnetic properties and are very attractive as model systems for theoretical investigations of magnetic ordering in rare-earth insulators with the competition of dipole-dipole and weak exchange interactions [43–53]. The ground configuration of RE^{3+} ions is $4f^n5s^25p^6$. The rare-earth trifluorides are paramagnetic in almost the whole temperature range due to weak exchange interactions between rare-earth ions and shielding effect of the $4f$ shell by the outer $5s$ and $5p$ shells. Among some rare earth trifluorides, magnetic ordering appears at temperature values of the order of 1 K. Several studies of the magnetic properties of heavy rare-earth trifluorides have been conducted in the past. According to the magnetization and specific heat measurements, ferromagnetic domains are induced in TbF$_3$ and DyF$_3$ at temperatures under $T_C = 3.95$ K [43] and 2.53 K [44], respectively, due to magnetic dipole-dipole interactions among the rare-earth ions. The antiferromagnetically ordered state of Ho^{3+} magnetic moments occurs in HoF$_3$ at temperature $T_N = 0.53$ K [45]. The antiferromagnetic phase was also found in ErF$_3$ from the neutron diffraction study at $T_N = 1.05$ K [48].

The magnetism of Yb$_x$Y$_{1-x}$F$_3$ compounds comes from the present Yb^{3+} ions. A free Yb^{3+} ion has electronic configuration $4f^{13}$ with one hole in almost filled $4f$ shell, ground multiplet ^{2}F$_{7/2}$ ($L = 4$, $S = 1/2$, $J = 7/2$) and the first exited multiplet ^{2}F$_{5/2}$. The energy splitting between

3

$^2F_{7/2}$ and $^2F_{5/2}$ is about 10000 cm^{-1}, which is the highest splitting among all rare-earth elements. Because of this, the excited multiplet $^2F_{5/2}$ does not influence significantly to the magnetic properties. The free Yb^{3+} ion ground level $^2F_{7/2}$ is an 8-fold degenerate term that is partially split by the ligand field. Under the effect of crystal fields that have symmetry lower than cubic, the Yb^{3+} ground level $^2F_{7/2}$ splits into the four Kramer's doublets. Hence, we should include this splitting in the analysis of the magnetic properties of Yb$_x$Y$_{1-x}$F$_3$ compounds for the entirely measured temperature range.

In the following study, we present the synthesis of Yb$_x$Y$_{1-x}$F$_3$ (x = 0, 0.01, 0.03, 0.05, 0.1, 0.25, 0.5, 0.7, 0.9, and 1) solid solutions. We have synthesized Yb^{3+} doped YF$_3$ samples by the fluorination of an appropriate mixture of oxides with ammonium hydrogen difluoride (NH$_4$HF$_2$). Fluorination of oxides with NH$_4$HF$_2$ is one of the most suitable methods to produce pure fluorides (oxygen-free) [54]. It is suitable due to its low price, easy usage, and the fact that the reaction with this agent does not require complex equipment. Fluorination of yttrium sesquioxides (or other rare-earth sesquioxides) with NH$_4$HF$_2$ in the air is taking place at temperatures near 300 °C according to the overall reaction [54]:

$$Y_2O_3 + 6NH_4HF_2 \rightarrow 2YF_3 + 6NH_4F + 3H_2O \,, \tag{1}$$

where H$_2$O, NH$_4$F, and remaining NH$_4$HF$_2$ evaporate and only YF$_3$ lefts [43]. Different intermediate compounds could appear during the fluorination reaction, and there is no established agreement about the actual flow of the reaction. During heating, fluorination of Y$_2$O$_3$ in the air probably takes place in two steps by forming two intermediate compounds, (NH$_4$)$_3$Y$_2$F$_9$ and NH$_4$Y$_2$F$_7$ [55].

The following work presents research on structural, morphological, and magnetic properties of Yb$_x$Y$_{1-x}$F$_3$ solid solutions, systems that have not yet been thoroughly investigated, as far as we know. Structural and microstructural analysis of obtained final samples was performed using X-ray powder diffraction (XRD), which is one of the most used methods due to its simplicity, speed and the fact that it can be applied to different classes of materials. Today's most used technique for refining crystal structure was presented by Hugo M. Rietveld in 1969 [56]. This method becomes widely used not only for structure refinement but also for different kinds of analyses, such as quantitative phase analysis, measurements of microstrain and crystallite size, stacking and twin faults. Refinement of the crystal structure of Yb$_x$Y$_{1-x}$F$_3$ solid solutions is necessary to show that single-phase samples are obtained and to monitor the changes in structural and microstructural parameters with changes in the concentration of the ytterbium.

2. Experimental

All starting chemicals were from Sigma−Aldrich (purity of $\geq$ 98.5−99.99 %). The appropriate amounts of commercial Y_2O_3 and Yb_2O_3 were mixed with NH_4HF_2 according to the overall reaction:

$$(1-x)Y_2O_3 + xYb_2O_3 + 6NH_4HF_2 \rightarrow 2Yb_xY_{1-x}F_3 + 6NH_4F + 3H_2O. \tag{2}$$
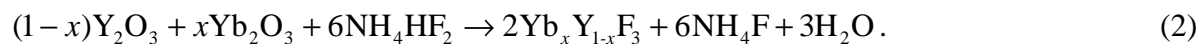
The obtained mixtures (for x = 0, 0.01, 0.03, 0.05, 0.1, 0.25, 0.5, 0.7, 0.9, and 1) were heated, first in the air at 170 °C for 20 h and then at 500 °C for 3 h in a reducing atmosphere (Ar-10% H_2).

We have checked the synthesized intermediate and final powder samples through XRD measurements on a Philips PW 1050 diffractometer that uses CuK_α radiation (λ = 1.54178 Å). XRD measurement conditions were: 2θ range 20–80° with a step of 0.05° and a counting time of 3 s. To refine the crystal structure of prepared samples, we have taken a new set of XRD measurements: 2θ range 10–120° with a step of 0.02° and a counting time of 12 s. We have done a Rietveld full-profile analysis [56] by the FullProf program [57] using the Thompson-Cox-Hastings pseudo-Voigt function. The effects of crystallite size and microstrain on peak broadening were treated using the spherical harmonics model and quadratic form model in reciprocal space, respectively. To estimate the instrumental peak broadening, we have used the resolution function determined from the XRD pattern of the LaB_6 standard.

The morphological properties of prepared samples were studied by scanning electron microscopy (SEM) on Jeol JSM-7600F. For SEM sample preparation, the powders were deposited on a graphite sample holder and coated with a Pt layer of 5 nm thickness using PECS Gatan 682. The elemental composition was investigated by field emission scanning electron microscopy (FESEM) on FEI Scios 2 microscope equipped with an energy dispersive X-ray spectrometer (EDX).

We have done the measurements of magnetic properties on an MPMS XL-5 SQUID magnetometer from Quantum Design. The magnetic susceptibility measurements were carried out within the 2–300 K temperature range at an applied magnetic field of 100 Öe. The field dependency of the isothermal magnetization was measured between -50 and 50 kÖe, at various temperatures (2, 5, 10, 20, 50, 100, 150, 200, and 300 K).

3. Results and discussion

3.1. Synthesis, structural and microstructural properties

The samples obtained from the first stage of synthesis in the air at 170 °C were analyzed by XRD (Fig. 2), and that products correspond to a complete phase formation of $(NH_4)_3(Yb_xY_{1-x})_2F_9$ (PCPDF: 43-0840). The SEM image of the representative $(NH_4)_3Yb_{0.02}Y_{1.98}F_9$ sample synthesized at 170 °C is presented in Fig. 3. Examined powders are composed of irregularly formed particles with average sizes of about 160 nm. Additionally, particles strongly aggregate and form larger structures.
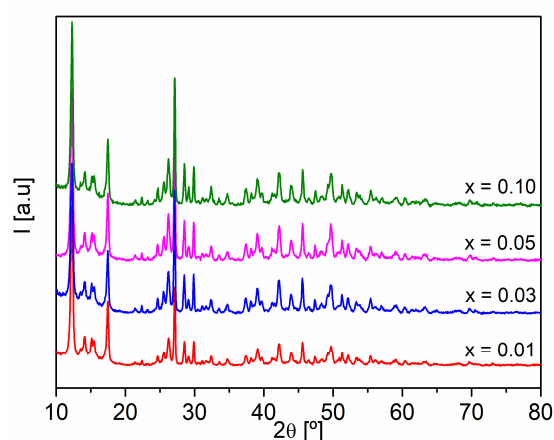
Fig. 2. XRD patterns of samples obtained at 170 °C for 20 h, intermediates $(NH_4)_3(Yb_xY_{1-x})_2F_9$ (x = 0.01, 0.03, 0.05 and 0.1).
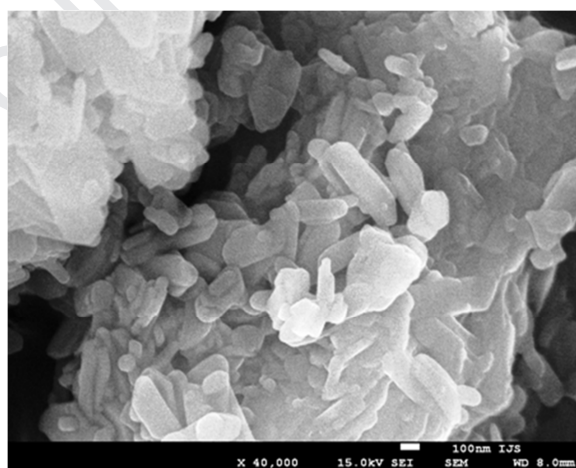
Fig. 3. SEM image of a sample $(NH_4)_3Yb_{0.02}Y_{1.98}F_9$.

In the second stage of the synthesis, the previously obtained products were heated in a reducing atmosphere (Ar-10% H_2) at 500 °C for 3 h. The XRD patterns of the final synthesized polycrystalline samples $Yb_xY_{1-x}F_3$ (x = 0, 0.01, 0.03, 0.05, 0.1, 0.25, 0.5, 0.7, 0.9, and 1) comprise only reflections of the β-YF$_3$ type orthorhombic crystal structure (Fig. 4).

6
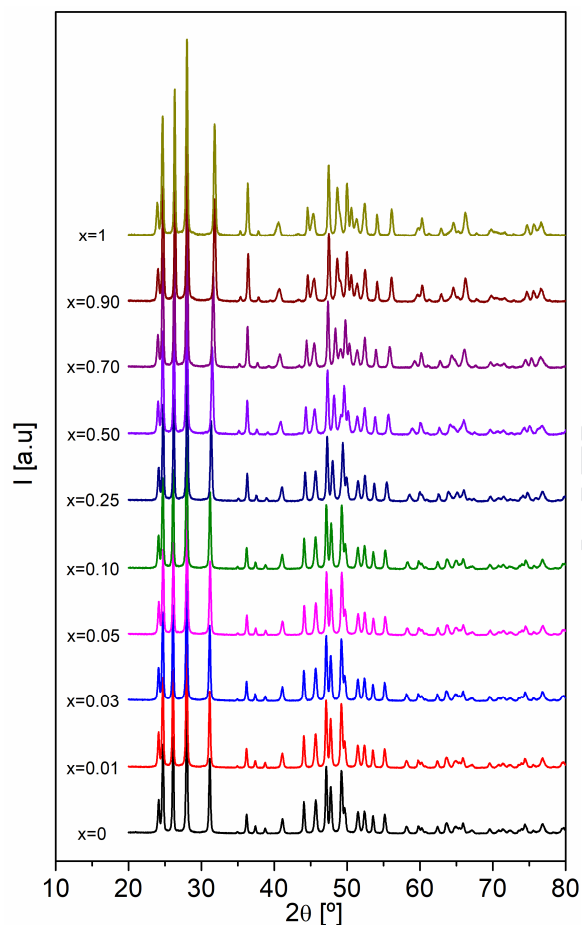
Fig. 4. XRD patterns of the final products $Yb_xY_{1-x}F_3$.

The crystal structure parameters of all $Yb_xY_{1-x}F_3$ samples were refined within the *Pnma* space group using the starting structural parameters from the work of Zalkin et al. [37]. The most important results of Rietveld refinements (crystallographic data, atomic and microstructural parameters) are given in Table 1 and Table 2. From these data, we can notice that an increase in the concentration x of Yb^{3+} ions causes a small decrease in the lattice parameters a and b and an increase in the lattice parameter c. The cell volume V decreases with increasing concentration of Yb^{3+} ions, which is usual behavior due to the small difference between the ionic radii of Yb^{3+} (0.98 Å) and Y^{3+} (1.015 Å) [58]. The final Rietveld plot for representative $Yb_{0.5}Y_{0.5}F_3$ is shown in Fig. 5.

During the Rietveld analysis, we observed an anisotropic peak broadening for all samples of solid solutions. At first, only anisotropic crystallite size and isotropic microstrain influence on peak broadening were considered, but refinement was not good enough. To achieve a better refinement, we included a model of a quadratic form in reciprocal space due to anisotropic microstrain. The calculated crystallite size is about 50 nm with a small degree

of anisotropy (anisotropy of shape), while all samples of solid solutions (including end-members) have significant microstrain (Table 2). Also, the microstrain present in samples is highly anisotropic, with much larger values of microstrain along different directions lying in the a–c plane than microstrain along the b-axis. The reason for such anisotropic microstrain lies in the fact that cations have a planar alignment in layers perpendicular to the b-axis and that there is only one positional parameter of fluorine ions at $8d$ general positions that can relax along the b-axis [59]. For that reason, any stress is mainly relaxed by displacements in the a–c plane. Anisotropic microstrain is illustrated by the graphical representation of the three-dimensional microstrain distribution (inset in Fig. 5).

**Table 1**

Crystallographic data of $Yb_xY_{1-x}F_3$ samples.

x:	0	0.01	0.03	0.05	0.1
a [Å]	6.35789(8)	6.35588(8)	6.35385(8)	6.35031(8)	6.34243(9)
b [Å]	6.86070(9)	6.85937(9)	6.85765(9)	6.85684(9)	6.85236(10)
c [Å]	4.40642(6)	4.40623(6)	4.40528(6)	4.40764(6)	4.40841(6)
Cell volume, V [Å^3]	192.206(4)	192.100(4)	191.949(4)	191.922(4)	191.592(5)
Formula units per cell, Z	4	4	4	4	4
Profile R-factors:					
R_{wp}	8.68 %	8.64 %	8.49 %	8.46 %	8.43 %
R_{exp}	7.02 %	7.16 %	7.29 %	7.34 %	7.48 %
Bragg R-factor, R_B	2.33 %	2.35 %	2.26 %	2.14 %	2.11 %
Chi^2	1.53	1.46	1.36	1.33	1.27
x:	0.25	0.5	0.7	0.9	1
a [Å]	6.31819(9)	6.27514(9)	6.24404(8)	6.21204(8)	6.19720(8)
b [Å]	6.84159(11)	6.82266(11)	6.80698(11)	6.79399(11)	6.78624(10)
c [Å]	4.41657(7)	4.43118(7)	4.43973(7)	4.45482(7)	4.45921(7)
Cell volume, V [Å^3]	190.913(5)	189.712(5)	188.702(5)	188.013(5)	187.535(5)
Formula units per cell, Z	4	4	4	4	4
Profile R-factors:					
R_{wp}	8.54 %	7.68 %	7.75 %	7.64 %	7.95 %
R_{exp}	7.59 %	7.51 %	7.27 %	7.07 %	6.97 %
Bragg R-factor, R_B	2.21 %	2.25 %	2.36 %	2.40 %	2.35 %
Chi^2	1.26	1.05	1.14	1.17	1.30

Standard deviations are given in parentheses.

8

Table 2

The refined values of the atomic parameters and microstructural parameters of $Yb_xY_{1-x}F_3$ samples.

x:		0	0.01	0.03	0.05	0.1
Y, Yb (4c)	x	0.36774(4)	0.36771(4)	0.36782(3)	0.36776(3)	0.36762(4)
	z	0.05883(5)	0.05875(5)	0.05878(5)	0.05855(5)	0.05835(5)
	B_{iso} (Å^2)	1.871(7)	1.914(7)	1.910(7)	1.876(7)	1.959(7)
F (4c)	x	0.5231(2)	0.5232(2)	0.5227(2)	0.5230(2)	0.5231(2)
	z	0.5918(3)	0.5920(3)	0.5918(3)	0.5921(9)	0.5933(3)
	B_{iso} (Å^2)	1.88(3)	1.93(3)	1.92(3)	1.89(3)	1.99(3)
F (8d)	x	0.1648(2)	0.1648(2)	0.1643(2)	0.1642(2)	0.1641(2)
	y	0.06283(11)	0.06261(10)	0.06229(10)	0.06252(10)	0.06249(11)
	z	0.3737(2)	0.3739(2)	0.3737(2)	0.3736(2)	0.3732(2)
	B_{iso} (Å^2)	2.04(2)	2.09(2)	2.08(2)	2.11(2)	2.12(2)
Average crystallite size (nm)		48	50	48	47	47
Average maximum microstrain (%)		0.16	0.16	0.16	0.17	0.17
x:		0.25	0.5	0.7	0.9	1
Y, Yb (4c)	x	0.36763(4)	0.36725(3)	0.36710(4)	0.36686(4)	0.36683(1)
	z	0.05727(5)	0.05554(4)	0.05430(5)	0.05303(5)	0.05240(2)
	B_{iso} (Å^2)	1.926(8)	1.953(7)	1.938(7)	1.926(7)	1.889(2)
F (4c)	x	0.5236(2)	0.5239(2)	0.5244(2)	0.5246(3)	0.52574(11)
	z	0.5946(4)	0.5994(4)	0.6029(4)	0.6076(4)	0.6060(2)
	B_{iso} (Å^2)	1.98(4)	2.02(4)	2.02(5)	2.02(5)	2.05(2)
F (8d)	x	0.1642(2)	0.1638(2)	0.1643(2)	0.1636(3)	0.16435(11)
	y	0.06246(12)	0.06231(12)	0.06233(14)	0.06271(2)	0.06258(6)
	z	0.3720(2)	0.3698(2)	0.3674(2)	0.3663(3)	0.36507(12)
	B_{iso} (Å^2)	2.14(3)	2.05(3)	1.86(3)	1.82(4)	1.82(2)
Average crystallite size (nm)		50	52	54	51	56
Average maximum microstrain (%)		0.23	0.29	0.27	0.25	0.24

Standard deviations are given in parentheses.
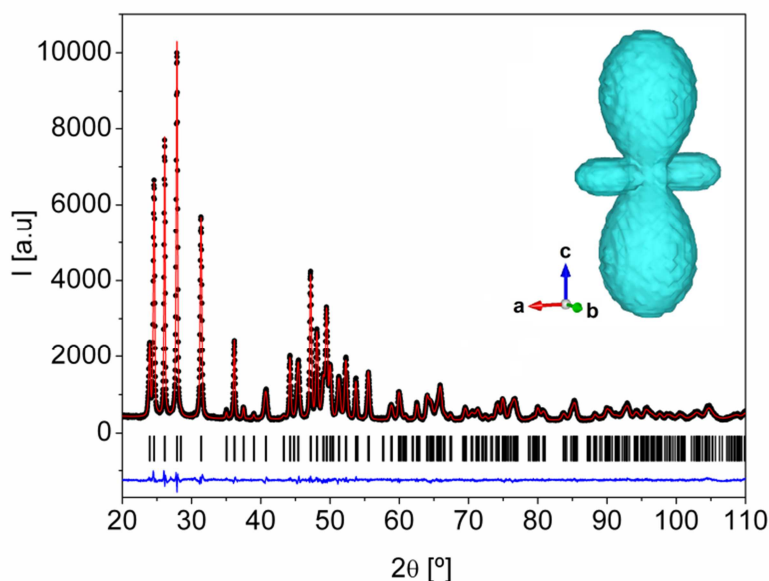
Fig. 5. (Color online） The final Rietveld plot for $Yb_{0.5}Y_{0.5}F_3$ sample: dots represent observed intensities; solid red line represents calculated intensities; bottom blue line shows the differences between the observed and calculated intensities and the vertical bars indicate the Bragg peaks. *Inset*: The graphical representation of the three-dimensional microstrain distribution.

Morphology and particle size of the samples prepared at 500 °C were investigated using the scanning electron microscopy. The SEM images of the representative samples are presented in Fig. 6. There is a visible difference between the morphologies of the final products and the product obtained in the intermediary phase (Fig. 2). Strongly agglomerated particles of irregular shape are also present in the final samples, but they aggregate in some more or less regular geometrical structures of about 1–3 μm in size. All samples prepared at 500 °C have particles with comparable morphology and sizes of 60–180 nm.
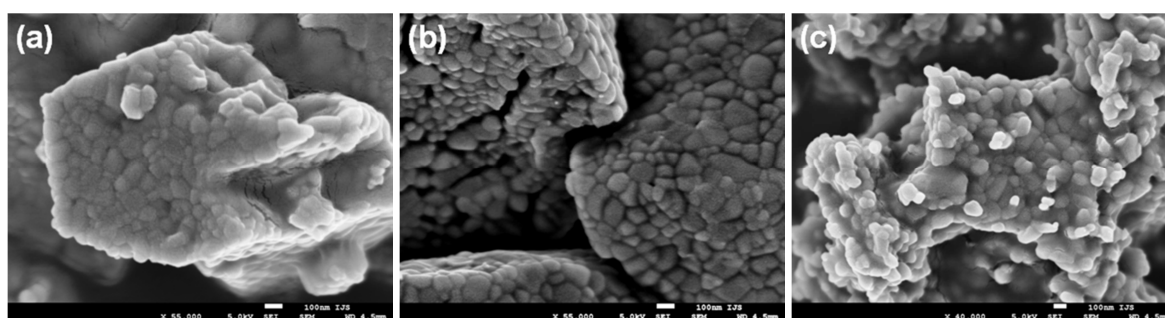
Fig. 6. SEM images of $Yb_xY_{1-x}F_3$ samples: (a) $x = 0.01$, (b) $x = 0.5$ and (c) $x = 1$.

To determine and confirm the compositions of synthesized $Yb_xY_{1-x}F_3$ samples, we performed the EDX analysis. The results of EDX analysis are presented in Table 3. Based on

this analysis, we calculated the compositions of the synthesized samples, and the obtained results are equal to the initial target compositions within the limits of standard deviations.

Table 3

Elemental analysis of $Yb_xY_{1-x}F_3$ samples.

Sample	Yb [at%]	Y [at%]	F [at%]	EDX composition
YF_3	-	25.2(3)	74.8(9)	$YF_{2.96(5)}$
$Yb_{0.01}Y_{0.99}F_3$	0.3(1)	24.5(3)	75.2(9)	$Yb_{0.012(4)}Y_{0.988(4)}F_{3.03(5)}$
$Yb_{0.03}Y_{0.97}F_3$	0.8(1)	24.4(3)	74.8(9)	$Yb_{0.032(4)}Y_{0.968(4)}F_{2.97(6)}$
$Yb_{0.05}Y_{0.95}F_3$	1.4(2)	23.6(3)	75.0(9)	$Yb_{0.056(8)}Y_{0.944(8)}F_{3.00(6)}$
$Yb_{0.10}Y_{0.90}F_3$	2.8(2)	21.7(3)	75.5(9)	$Yb_{0.114(7)}Y_{0.886(7)}F_{3.08(6)}$
$Yb_{0.25}Y_{0.75}F_3$	6.5(2)	18.8(3)	74.7(9)	$Yb_{0.257(7)}Y_{0.743(7)}F_{2.95(6)}$
$Yb_{0.50}Y_{0.50}F_3$	12.9(3)	12.5(3)	74.6(9)	$Yb_{0.508(8)}Y_{0.492(8)}F_{2.94(6)}$
$Yb_{0.70}Y_{0.30}F_3$	17.4(3)	7.9(2)	74.7(9)	$Yb_{0.688(7)}Y_{0.312(7)}F_{2.95(6)}$
$Yb_{0.90}Y_{0.10}F_3$	22.8(3)	2.7(2)	74.5(9)	$Yb_{0.894(7)}Y_{0.106(7)}F_{2.92(5)}$
YbF_3	25.3(3)	-	74.7(9)	$YbF_{2.95(5)}$

Standard deviations are given in parentheses.

3.2. Magnetic properties

The temperature-dependent inverse paramagnetic susceptibilities deviate from the Curie-Weiss behavior for all samples (Fig. 7). This kind of behavior is a result of the crystal field effect on the Yb^{3+} ground state. As mentioned before, Yb^{3+} ions are placed at position $4c$ with C_s symmetry. Therefore the crystal field of the same symmetry causes the splitting of 8-fold degenerate ground level $^2F_{7/2}$ into four Kramer's doublets. The effective magnetic quantum number $\pm M_{ieff}$ ($i = 0$, 1, 2, and 3) assigned to each doublet represents a linear combination of the magnetic quantum numbers in a free ion. As the temperature changes, the population of Kramer's doublets changes, and this leads to a temperature-dependent effective magnetic moment. In the present case, the following equation describes the dependency of the magnetic susceptibility on temperature [60]:

$$\chi = \frac{xN_A g_J^2 \mu_0 \mu_B^2}{k_B(T - \theta)} \frac{\sum_{i=0}^{3} M_{ieff}^2 \exp(-E_i / k_B T)}{\sum_{i=0}^{3} \exp(-E_i / k_B T)} , \tag{3}$$

where x is the concentration of Yb^{3+} ions, N_A is the Avogadro constant, $g_J = 8/7$ is the Landé splitting factor, μ_0 is the vacuum magnetic permeability, μ_B is the Bohr magneton, M_{ieff} ($i = 0$, 1, 2, and 3) are the effective magnetic quantum numbers assigned to Kramer's doublets, E_i is the energy gap between the ground ($i = 0$) and i-th excited doublet ($i = 1$, 2 and 3), k_B is Boltzmann's constant and θ is the Curie-Weiss paramagnetic temperature.

At low temperatures $T < 3$ K, only the lowest Kramer's doublet is populated, and in this temperature region, the paramagnetic susceptibility follows the Curie-Weiss law (insets in Fig. 7). Equation (3) becomes [60]:

$$\chi = \frac{x N_A g_J^2 \mu_0 \mu_B^2 M_{0eff}^2}{k_B (T - \theta)} . \tag{4}$$

By fitting equation (4) to the low-temperature experimental data, we have obtained the values of M_{0eff} and θ (Table 4). The Curie-Weiss paramagnetic temperature θ obtained from the low-temperature paramagnetic susceptibility is a result of weak exchange interactions between Yb^{3+} ions and not of crystal field effect. For all samples, θ has negative values, which indicates a predominance of antiferromagnetic exchange interactions. The $\theta(x)$ dependency (Fig. 8) is linear, which shows that magnetic Yb^{3+} ions do not tend to cluster [60]. The remaining six parameters were determined from the fit of equation (3) to the experimental data within the entirely measured temperature range, where the values of M_{0eff} and θ were from the fit to the low-temperature data (Table 4). The obtained values of M_{ieff} and E_i show good agreement between values for different ytterbium concentrations x, and we have calculated their mean values (Table 4). According to the investigated literature [61–63], there are very few available experimental values of the energy sublevels of Yb^{3+} ions in YF_3 with which we can compare our obtained energy values E_i. The only available experimental energy splitting of the $^2F_{7/2}$ level is from luminescence measurement, and its value is about 167 K [62]. The obtained maximum energy splitting of ground level $^2F_{7/2}$ (E_3/k_B) in our most diluted samples ($x = 0.01$ and 0.03) is in a remarkable agreement with this energy splitting measured from the luminescence spectra.
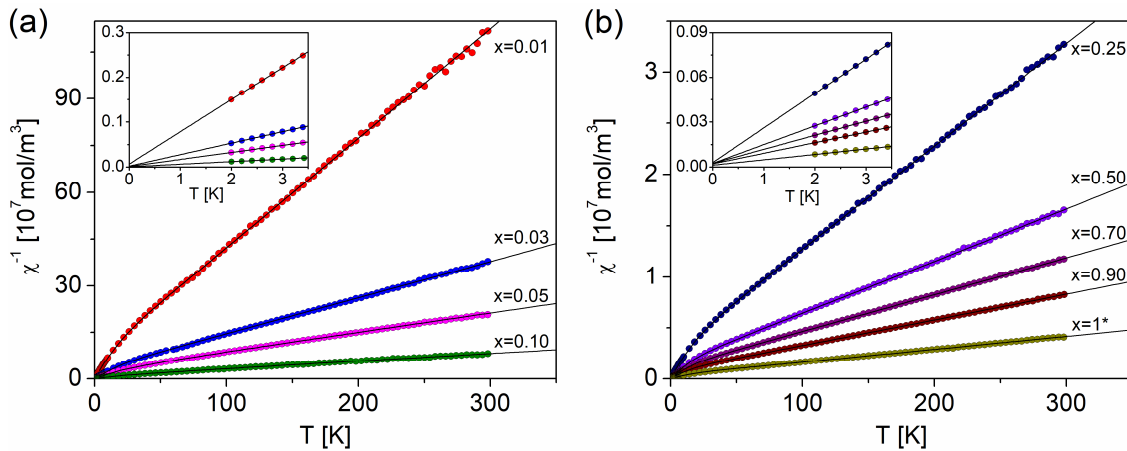
Fig. 7. (Color online) The inverse susceptibilities for $Yb_xY_{1-x}F_3$ samples over the full temperature range: (a) $x = 0.01$, 0.03, 0.05 and 0.1, (b) $x = 0.25$, 0.5, 0.7, 0.9 and 1^*. The full lines represent the calculated curves. *Experimental data and

corresponding calculated curve for sample $x = 1$ are multiplied by 0.5 for better visibility. *Insets*: The inverse low-temperature susceptibilities, where the full lines represent fits of the Curie-Weiss law.
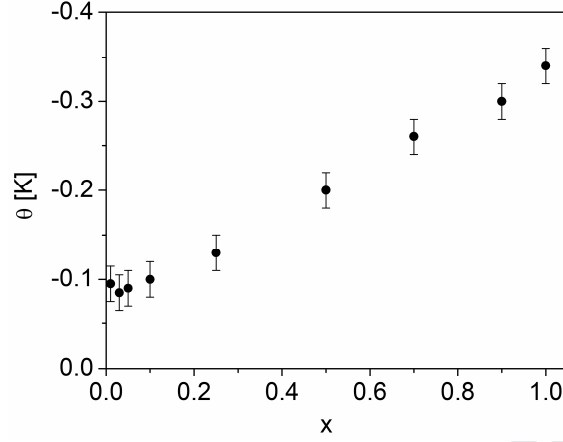
Fig. 8. Curie-Weiss paramagnetic temperature θ obtained from the low-temperature region ($T < 3$ K) for Yb$_x$Y$_{1-x}$F$_3$ samples.

Table 4

The effective magnetic quantum numbers M_{ieff} of the Kramer's doublets, their crystal field energies E_i/k_B and Curie-Weiss paramagnetic temperatures θ for Yb$_x$Y$_{1-x}$F$_3$.

| x:	0.01	0.03	0.05	0.1	0.25
M_{0eff}	1.506(5)	1.459(6)	1.446(6)	1.691(10)	1.677(12)
M_{1eff}	1.738(9)	1.719(8)	1.729(8)	1.89(3)	1.981(8)
M_{2eff}	2.715(6)	2.692(9)	2.775(6)	3.234(18)	3.270(10)
M_{3eff}	2.394(14)	2.479(10)	2.852(7)	3.111(16)	2.89(6)
E_1/k_B [K]	14.0(3)	15.9(3)	16.9(3)	13.0(10)	14.9(3)
E_2/k_B [K]	64.2(3)	65.3(4)	69.5(2)	60.4(6)	66.5(4)
E_3/k_B [K]	146(8)	157(3)	245(2)	213(5)	197(2)
θ [K]	-0.095(20)	-0.085(18)	-0.09(2)	-0.098(24)	-0.129(15)
x:	0.5	0.7	0.9	1	Mean value
M_{0eff}	1.612(5)	1.574(4)	1.600(5)	1.505(5)	1.563(6)
M_{1eff}	1.977(8)	2.026(11)	2.111(13)	1.966(8)	1.904(11)
M_{2eff}	3.294(10)	3.379(10)	3.572(10)	3.412(10)	3.149(10)
M_{3eff}	2.822(4)	2.733(4)	2.925(6)	2.729(4)	2.771(14)
E_1/k_B [K]	16.2(2)	17.7(3)	17.4(2)	16.7(2)	15.9(3)
E_2/k_B [K]	66.8(3)	73.2(3)	70.7(3)	66.8(3)	67.0(3)
E_3/k_B [K]	188(2)	252(3)	215(3)	197(3)	201(3)
θ [K]	-0.197(17)	-0.26(2)	-0.30(2)	-0.34(2)	

Standard deviations are given in parentheses.

According to the literature, crystal field splitting of the ground term of the rare earth ions also bares an influence on heat capacity behavior. Measurements of the heat capacity C_p in a low-temperature range from 5 to 350 K show a small and smooth increase in C_p values, with no transitions [64]. The low-temperature heat capacity of rare earth fluorides can be

represented as a sum of two components: the lattice component C_{lat}, that occurs due to the vibration of the ions in the crystal and an excess component C_{exc}, which is a consequence of the splitting of the ground level due to the action of the ligand field. This excess contribution is known as Schottky's contribution or Schottky anomaly [39]. The high-temperature heat capacity can, in analogy with the low-temperature case, also be written as a sum of C_{lat} and C_{exc}. The difference is in the origin of the C_{lat} which, in contrast to the low-temperature case, does not arise from the harmonic vibrations, but arises from the influence of the anharmonic vibrations, as well as the thermal dilatation of lattice and of the thermally induced vacancies in the lattice. The values of the heat capacity are smooth and continuous in the whole temperature range, except at the temperatures at which transitions occur (from β-YF$_3$ to α-YF$_3$ structure and melting point), where heat capacity jumps can be observed [40,65,66].

Fig. 9 shows the field dependencies of magnetization $M(H)$ at 2 K. For all samples, the $M(H)$ curves show no hysteresis, and there is no saturation of magnetization up to 50 kÖe, which is expected for paramagnetic systems. The Langevin function $L(y)$ describes the magnetization of a classical paramagnetic material [67]:

$$M = M_S L(y) = M_S \left[\coth y - \frac{1}{y} \right], \tag{5}$$

where M_S is the maximum magnetization that could be measured when all the magnetic moments are aligned, $y = \mu B/k_B T$, μ is the magnetic moment of an ion, B is the magnetic field and k_B is Boltzmann's constant. We have fitted the classical Langevin function successfully to all experimentally observed $M(H)$ curves, which proves that prepared Yb$_x$Y$_{1-x}$F$_3$ samples are paramagnetic.
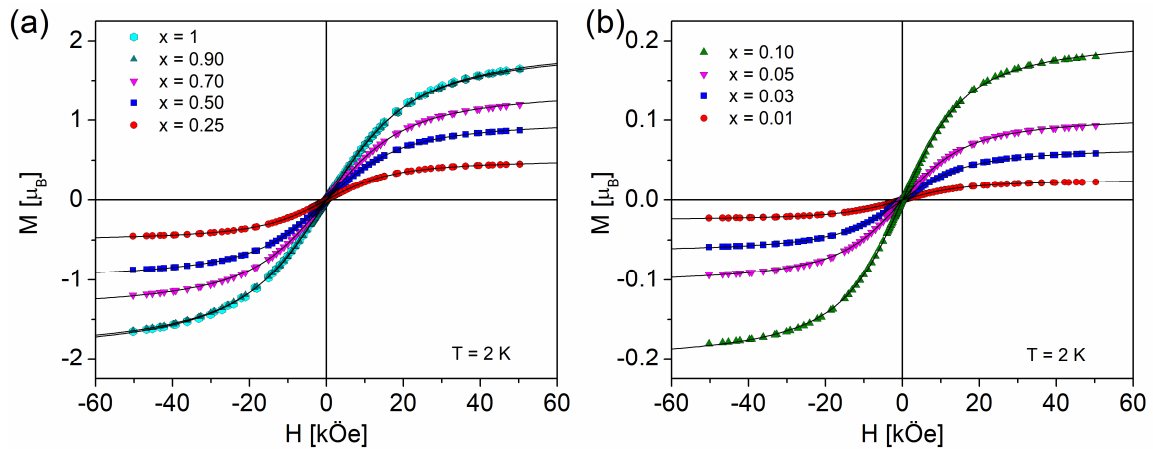
Fig. 9. (Color online) The isothermal magnetization vs. magnetic field data measured at 2 K for Yb$_x$Y$_{1-x}$F$_3$ samples: (a) $x = 1$, 0.9, 0.7, 0.5 and 0.25, (b) $x = 0.1$, 0.05, 0.03 and 0.01. The full lines represent the calculated curves.

For $Yb_{0.7}Y_{0.3}F_3$ and $Yb_{0.9}Y_{0.1}F_3$ samples, field dependencies of the isothermal magnetization were measured at various temperatures (2, 5, 10, 20, 50, 100, 150, 200, and 300 K) and the obtained $M(H/T)$ curves are shown in Fig. 10.
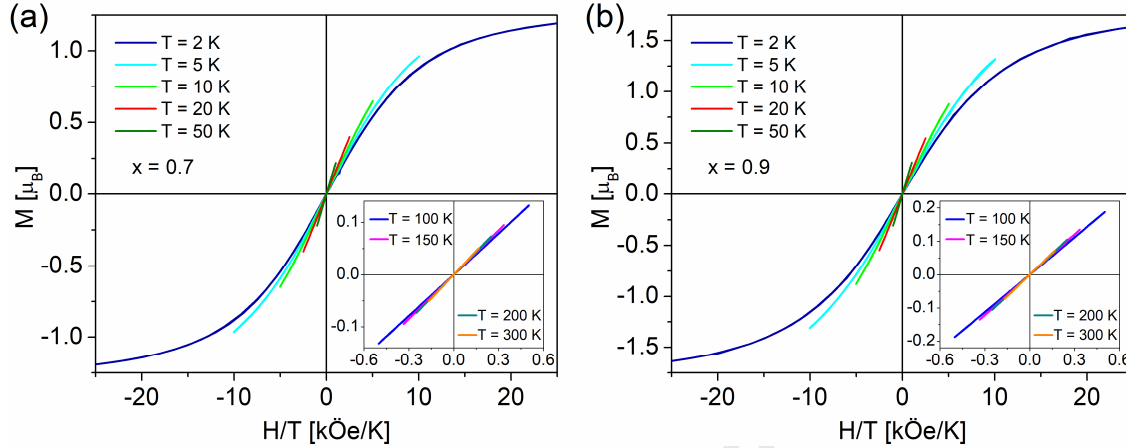
Fig. 10. (Color online) The isothermal magnetization $M(H/T)$ at different temperatures for (a) $Yb_{0.7}Y_{0.3}F_3$ and (b) $Yb_{0.9}Y_{0.1}F_3$.

When the effective magnetic moment does not change with temperature, the experimental curves $M(H/T)$ obtained at different temperatures should overlap [68], as is the case when only the lowest Kramer's doublet of Yb^{3+} ions is populated in the entire measured temperature interval. In our samples, $M(H/T)$ curves measured at different temperatures do not overlap. Behavior like this occurs due to the thermal population or depopulation of Kramer's doublets with increasing temperatures, which leads to the temperature-dependent effective magnetic moment.

4. Conclusion

The polycrystalline $Yb_xY_{1-x}F_3$ samples analyzed in this work were synthesized by the fluorination of a mixture of Y_2O_3 and Yb_2O_3 with NH_4HF_2. The fluorination takes place in stages, first in the air at 170 °C by the formation of $(NH_4)_3(Yb_xY_{1-x})_2F_9$ and then at 500 °C in a reducing atmosphere by the formation of final solid solutions. XRD measurements show that all final synthesized samples crystallize in the same orthorhombic crystal structure of a β-YF_3 type. Increasing the concentration x of Yb^{3+} ions in samples causes only a small change in the lattice parameters, due to the small difference in the ionic radii of Yb^{3+} and Y^{3+} ions. According to the microstructural analysis, the crystallite size of the final samples is about 50

15

nm with a low degree of anisotropy, while all samples of solid solutions possess a significant microstrain with a high degree of anisotropy.

The temperature dependency of the inverse paramagnetic susceptibility of all $Yb_xY_{1-x}F_3$ samples departs from the Curie-Weiss behavior and can be fitted by the equation (3). This fit enables us to determine the effective magnetic quantum numbers M_{ieff} of the four Kramer's doublets of Yb^{3+} ion, as well as the values for the energy gaps E_i between the ground and i-th excited doublet. We believe that we report for the first time experimentally determined complete crystal field splitting of the ground ($^2F_{7/2}$) manifold of Yb^{3+} in the YF_3 host (C_s site). The obtained maximum energy splitting of ground level $^2F_{7/2}$ in our most diluted samples is in agreement with the only available experimental value from the literature [62].

The Curie-Weiss paramagnetic temperature θ determined from the low-temperature paramagnetic susceptibility has negative and small values for all samples, indicating a predominance of the antiferromagnetic exchange interaction. The dependency of the parameter θ is linear with the concentration of Yb^{3+} ions, which shows the absence of the clustering of Yb^{3+} ions. All experimentally observed $M(H)$ curves for all $Yb_xY_{1-x}F_3$ samples can be fitted by the classical Langevin function, which confirms the pure paramagnetic behavior at all measured temperatures (2–300 K).

Acknowledgments

References

[1]   C.R. Ronda, T. Jüstel, H. Nikol, Rare earth phosphors: fundamentals and applications, J. Alloys Compd. 275–277 (1998) 669–676.

[2]   P. Alemany, I.D.P.R. Moreira, R. Castillo, J. Llanos, Electronic, structural, and optical properties of host materials for inorganic phosphors, J. Alloys Compd. 513 (2012) 630–640.

[3]   C.E. Secu, C. Bartha, E. Matei, C. Negrila, A. Crisan, M. Secu, Gd^{3+} co-doping influence on the morphological, up-conversion luminescence and magnetic properties of $LiYF_4:Yb^{3+}/Er^{3+}$ nanocrystals, J. Phys. Chem. Solids. 130 (2019) 236–241.

[4]   C. Artini, F. Locardi, M. Pani, I. Nelli, F. Caglieris, R. Masini, J.R. Plaisier, G.A. Costa, Yb-doped $Gd_2O_2CO_3$: Structure, microstructure, thermal and magnetic

behaviour, J. Phys. Chem. Solids. 103 (2017) 59–66.

[5] A. Maurya, A. Bahadur, A. Dwivedi, A.K. Choudhary, T.P. Yadav, P.K. Vishwakarma, S.B. Rai, Optical properties of Er^{3+}, Yb^{3+} co-doped calcium zirconate phosphor and temperature sensing efficiency: Effect of alkali ions (Li^+, Na^+ and K^+), J. Phys. Chem. Solids. 119 (2018) 228–237.

[6] B. Zegaou, N. Benkhettou, D. Rached, A.H. Reshak, S. Benalia, Electronic structure of GdX_2 (X = Fe, Co and Ni) intermetallic compounds studied by the GGA+U method, Comput. Mater. Sci. 87 (2014) 172–177.

[7] T. Kushida, Energy transfer and coopertive optical transitions in rare-earth doped inorganic materials. I. Transition probability calculation, J. Phys. Soc. Japan. 34 (1973) 1318–1326.

[8] S.M. Saini, The role of f-states in the electronic and optical properties of rare-earth trifluorides (RF_3, R = Ce and Gd): a full potential study, J. Mater. Sci. 47 (2012) 7665–7670.

[9] S. Gai, C. Li, P. Yang, J. Lin, Recent Progress in Rare Earth Micro/Nanocrystals: Soft Chemical Synthesis, Luminescent Properties, and Biomedical Applications, Chem. Rev. 114 (2014) 2343–2389.

[10] F. Wang, X. Liu, Recent advances in the chemistry of lanthanide-doped upconversion nanocrystals, Chem. Soc. Rev. 38 (2009) 976–989.

[11] K. Riwotzki, M. Haase, Wet-Chemical Synthesis of Doped Colloidal Nanoparticles: YVO_4:Ln (Ln = Eu , Sm , Dy), J. Phys. Chem. B. 102 (1998) 10129–10135.

[12] M. Mitric, J. Blanusa, T. Barudzija, Z. Jaglicic, V. Kusigerski, V. Spasojevic, Magnetic properties of trivalent Sm ions in $Sm_xY_{2-x}O_3$, J. Alloys Compd. 485 (2009) 473–477.

[13] Z.K. Heiba, M.B. Mohamed, Structural and magnetic properties of Mn doped Ho_2O_3 nanocrystalline, J. Mol. Struct. 1102 (2015) 135–140.

[14] C.E. Secu, E. Matei, C. Negrila, M. Secu, The influence of the nanocrystals size and surface on the Yb/Er doped LaF_3 luminescence properties, J. Alloys Compd. 791 (2019) 1098–1104.

[15] R. Si, Y.-W. Zhang, L.-P. You, C.-H. Yan, Rare-earth oxide nanopolyhedra, nanoplates, and nanodisks, Angew. Chemie Iternational Ed. 44 (2005) 3256–3260.

[16] R. Si, Y.-W. Zhang, H.-P. Zhou, L.-D. Sun, C.-H. Yan, Controlled-synthesis, self-assembly behavoir, and surface-dependent optical properties of high-quality rare-earth oxide nanocrystals, Chem. Mater. 19 (2007) 18–27.

[17] L. He, L. Xia, Y. Yang, Q. Zheng, N. Jiang, C. Xu, Y. Liu, D. Lin, Morphology-controlled synthesis, growth mechanism and fluorescence of YF_3:Eu3+,Bi^{3+}, Mater. Res. Bull. 95 (2017) 483–490.

[18] F. Wang, Y. Han, C.S. Lim, Y. Lu, J. Wang, J. Xu, H. Chen, C. Zhang, M. Hong, X. Liu, Simultaneous phase and size control of upconversion nanocystals through lanthanide doping, Nature. 463 (2010) 1061–1065.

[19] Y.C. Cao, Synthesis of square gadolinium-oxide nanoplates, J. Am. Chem. Soc. 126 (2004) 7456–7457.

[20] S.-L. Zhong, Y. Lu, M.-R. Gao, S.-J. Liu, J. Peng, L.-C. Zhang, S.-H. Yu, Monodisperse mesocrystals of YF_3 and Ce^{3+}/Ln^{3+} (Ln = Tb, Eu) co-activated YF_3: Shape control synthesis, luminescent properties, and biocompatibility, Chem. - A Eur. J. 18 (2012) 5222–5231.

[21] H. Guan, C. Xu, X. Zhou, Y. Sheng, Y. Song, K. Zheng, Z. Shi, H. Zou, Control morphology, tunable multicolor and paramagnetic properties of GdF_3:RE^{3+} (RE = Tm, Dy, Eu) submicro structures, J. Alloys Compd. 725 (2017) 952–967.

[22] D. Naveena, T. Logu, K. Sethuraman, A.C. Bose, Significant enhancement of photo-physicochemical properties of Yb doped copper oxide thin films for efficient solid-state solar cell, J. Alloys Compd. 795 (2019) 187–196.

[23] A.J. Kenyon, Recent developments in rare-earth doped materials for optoelectronics, Prog. Quantum Electron. 26 (2002) 225–284.

[24] M. Nyk, R. Kumar, T.Y. Ohulchanskyy, E.J. Bergey, P.N. Prasad, High contrast in vitro and in vivo photoluminescence bioimaging using near infrared to near infrared up-conversion in Tm^{3+} and Yb^{3+} doped fluoride nanophosphors, Nano Lett. 8 (2008) 3834–3838.

[25] J. Zhou, Z. Liu, F. Li, Upconversion nanophosphors for small-animal imaging, Chem. Soc. Rev. 41 (2012) 1323–1349.

[26] S. Sivakumar, F.C.J.. M. Van Veggel, M. Raudsepp, Bright white light through up-conversion of a single NIR source from sol-gel-derived thin film made with Ln^{3+}-doped LaF_3 nanoparticles, J. Am. Chem. Soc. 127 (2005) 12464–12465.

[27] C. Li, C. Zhang, Z. Hou, L. Wang, Z. Quan, H. Lian, J. Lin, β-$NaYF_4$ and β-$NaYF_4$:Eu^{3+} microstructures: Morphology control and tunable luminescence properties, J. Phys. Chem. 113 (2009) 2332–2339.

[28] P. Ren, Y. Gao, Y. Hu, Y. Yang, D. Zhou, J. Qiu, Up-conversion luminescence of Er^{3+} ions in transparent oxyfluoride glass ceramics containing $Na(Gd_x,Y_{1-x})F_4$ nanocrystals, Mater. Res. Bull. 85 (2017) 47–51.

[29] Y.S. Zhao, H. Fu, F. Hu, A.D. Peng, J. Yao, Multicolor emission from ordered assemblies of organic 1D nanomaterials, Adv. Mater. 19 (2007) 3554–3558.

[30] P. Seth, G. Swati, D. Haranath, S.M.D. Rao, S. Aggarwal, A photoluminescence, thermoluminescence and electron paramagnetic resonance study of EFG grown europium doped lithium fluoride (LiF) crystals, J. Phys. Chem. Solids. 118 (2018) 53–61.

[31] S.K. Gupta, C. Reghukumar, K. Sudarshan, P.S. Ghosh, N. Pathak, R.M. Kadam, Orange-red emitting $Gd_2Zr_2O_7$:Sm^{3+}: Structure-property correlation , optical properties and defect spectroscopy, J. Phys. Chem. Solids. 116 (2018) 360–366.

[32] Q. Han, L. Yan, C. Zhang, M. Zhang, T. Zhang, H. Zheng, Influence of Au nanoparticles on luminescence property of YF_3 submicrostructures doped with Yb^{3+} and Ho^{3+} (Eu^{3+}) ions, J. Alloys Compd. 715 (2017) 322–328.

[33] I.A. Razumkova, Y.G. Denisenko, A.N. Boyko, D.A. Ikonnikov, A.S. Aleksandrovsky, N.O. Azarapin, O. V. Andreev, Synthesis and upconversion luminescence in LaF_3:Yb^{3+}, Ho^{3+}, GdF_3: Yb^{3+}, Tm^{3+} and YF_3:Yb^{3+}, Er^{3+} obtained from sulfide precursors, Zeitschrift Fur Anorg. Und Allg. Chemie. 645 (2019) 1393–1401.

[34] M. Runowski, S. Lis, Nanocrystalline rare earth fluorides doped with Pr^{3+} ions, J. Rare Earths. 34 (2016) 802–807.

[35] L.G. Jacobsohn, C.L. Mcpherson, L.C. Oliveira, C.J. Kucera, J. Ballato, E.G. Yukihara, Radioluminescence and thermoluminescence of rare earth doped and co-doped YF_3, Radiat. Meas. 106 (2017) 79–83.

[36] G. Murali, S. Kaur, Y.C. Chae, M. Ramesh, J. Kim, Y.D. Suh, D.K. Lim, S.H. Lee, Monodisperse, shape-selective synthesis of $YF_3:Yb^{3+}/Er^{3+}$ nano/microcrystals and strong upconversion luminescence of hollow microcrystals, RSC Adv. 7 (2017) 24255–24262.

[37] A. Zalkin, D.H. Templeton, The crystal structures of YF_3 and related compounds, J. Am. Chem. Soc. 75 (1953) 2453–2458.

[38] S.V. Stankus, R.A. Khairulin, K.M. Lyapunov, Thermal properties and phase transitions of heavy rare-earth fluorides, High Temp. – High Press. 32 (2000) 467–472.

[39] R.J.M. Konings, A. Kovács, Thermodynamic properties of the lanthanide(III) halides, in: K.A. Gschneidne Jr., J.-C.G. Bünzli, V.K. Pecharsky (Eds.), Handb. Phys. Chem. Rare Earths Vol. 33, Elsevier Science B.V., Amsterdam, 2003: pp. 147–248.

[40] Z. Kang, C. Robelin, M. He, P. Chartrand, Thermodynamic evaluation and optimization of the $(KF+YF_3)$, $(KCl+YCl_3)$ and (YF_3+YbF_3) binary systems, J. Chem Thermodinamics. 98 (2016) 242–253.

[41] K.F. Zmbov, J.L. Margrave, Mass Spectrometric studies of scandium, yttrium, lanthanum, and rare-earth fluorides, in: J.L. Margrave (Ed.), Mass Spectrom. Inorg. Chem., American Chemical Society, Washington, D.C., 1968: pp. 267–290.

[42] M. Darbandi, T. Nann, One-pot synthesis of YF_3@silica core/shell nanoparticles, Chem. Commun. (2006) 776–778.

[43] L. Holmes, H.J. Guggenheim, G.W. Hull, Spin-flip behavior in a ferromagnet, TbF_3, Solid State Commun. 8 (1970) 2005–2007.

[44] L.M. Holmes, F. Hulliger, H.J. Guggenheim, J.P. Maita, Specific heat of a dipolar-coupled Ising ferromagnet $LiTbF_4$, Phys. Lett. A. 50 (1974) 163–164.

[45] B. Bleaney, J.F. Gregg, R.W. Hill, M. Lazzouni, M.J.M. Leask, M.R. Wells, Magnetic and thermal properties of HoF_3-ordering in a singlet ground state, J. Phys. C Solid State Phys. 49 (1988) 2721–2734.

[46] P.J. Brown, J.B. Forsyth, P.C. Hansen, M.J.M. Leask, R.C.C. Ward, M.R. Wells, Neutron diffraction determination of magnetic order in holmium trifluoride, HoF_3, J. Phys. Condens. Matter. 2 (1990) 4471–4484.

[47] G. Liu, B. Yuan, N. Zhang, X. Gong, Calculation of the magnetic susceptibility and the Verdet constant in neodymium trifluoride, J. Appl. Phys. 78 (1995) 4054–4059.

[48] K. Krämer, H. Romstedt, H.U. Güdel, P. Fischer, A. Murasik, M.T. Fernandez-Diaz, Three dimensional magnetic structure of ErF_3, Eur. J. Solid State Inorg. Chem. 33 (1996) 273–283.

[49] J. Blanusa, M. Mitric, V. Kusigerski, V. Spasojevic, Z. Jagličić, J. Pirnat, Z. Trontelj, Magnetic properties of $Er_xY_{1-x}F_3$ solid solutions, Solid State Commun. 133 (2005) 157–161.

[50]   A. V. Savinkov, D.S. Irisov, B.Z. Malkin, K.R. Safiullin, H. Suzuki, M.S. Tagirov, D.A. Tayurskii, Anisotropic magnetic susceptibility and crystal field analysis in the Van Vleck paramagnet PrF_3, J. Phys. Condens. Matter. 18 (2006) 6337–6347.

[51]   A. V. Savinkov, S.L. Korableva, A.A. Rodionov, I.N. Kurkin, B.Z. Malkin, M.S. Tagirov, H. Suzuki, K. Matsumoto, S. Abe, Magnetic properties of Dy^{3+} ions and crystal field characterization in $YF_3:Dy^{3+}$ and DyF_3 single crystals, J. Phys. Condens. Matter. 20 (2008) 485220.

[52]   H.G. Liu, W.C. Zheng, Theoretical investigations of the optical and EPR spectra for trivalent cerium and ytterbium ions in orthorhombic YF_3 crystal, Phys. B. 496 (2016) 15–19.

[53]   A.V. Savinkov, B.F. Gabbasov, O.A. Morozov, A.G. Kiiamov, M.S. Tagirov, Study of the crystal field and rare-earth magnetism in $YF_3:Yb^{3+}$, Magn. Reson. Solids. 19 (2017) 1–5.

[54]   A. Mukherjee, A. Awasthi, S. Mishra, N. Krishnamurthy, Studies on fluorination of Y_2O_3 by NH_4HF_2, Thermochim. Acta. 520 (2011) 145–152.

[55]   A. Mukherjee, S. Mishra, N. Krishnamurthy, Thermogravimetric studies and kinetics of decomposition of ammonium yttrium fluoride, React. Kinet. Mech. Catal. 103 (2011) 53–70.

[56]   H.M. Rietveld, A profile refinement method for nuclear and magnetic structures, J. Appl. Crystallogr. 2 (1969) 65–71.

[57]   J. Rodríguez-Carvajal, Recent advances in magnetic structure determination by neutron powder diffraction, Phys. B. 192 (1993) 55–69.

[58]   R.D. Shannon, C.T. Prewitt, Revised values of effective ionic radii, Acta Crystallogr. Sect. B. 26 (1970) 1046–1048.

[59]   E. Talik, P. Zajdel, A. Guzik, D. Skrzypek, L. Lipińska, M. Michalska, Electronic and crystal structure, EPR and magnetic investigations of YF_3:1%RE (RE = Pr, Ho, Er and Tm) and LaF_3:1%Pr nanocrystals, J. Alloys Compd. 616 (2014) 556–568.

[60]   M. Mitric, B. Antic, M. Balanda, D. Rodic, M.L. Napijalo, An X-ray diffraction and magnetic susceptibility study of $Yb_xY_{2-x}O_3$, J. Phys. Condens. Matter. 9 (1997) 4103–4111.

[61]   H. Kuroda, S. Shionoya, T. Kushida, Mechanism and controlling factors of infrared-to-visible conversion process in Er^{3+} and Yb^{3+}-doped phosphors, J. Phys. Soc. Japan. 33 (1972) 125–141.

[62]   M.P. Davydova, B.N. Kazakov, A.L. Stolov, Parameters of the crystal field acting on rare-earth ions in YF_3 crystal, Sov. Phys. - Solid State. 20 (1978) 1378–1382.

[63]   C.A. Morrison, R.P. Leavitt, Spectroscopic properties of triply ionized lanthanides in transparent host crystals, in: K.A. Gschneidner, L. Eyring (Eds.), Handb. Phys. Chem. Rare Earths, North-Holland Publishing Company, Amsterdam, 1982: pp. 461–692.

[64]   H.E. Flotow, P.A.G. O'Hare, Thermodynamics of the lanthanide trifluorides. IV. The heat capacities of gadolinium trifluoride GdF_3, lutetium trifluoride LuF_3, and yttrium trifluoride YF_3 from 5 to 350 °K, J. Chem. Phys. 74 (1981) 3046–3055.

[65]   F.H. Spedding, B.J. Beaudry, D.C. Henderson, J. Moorman, High temperature

enthalpies and related thermodynamic functions of the trifluorides of Sc, Ce, Sm, Eu, Gd, Tb, Dy, Er, Tm, and Yb, J. Chem. Phys. 60 (1974) 1578–1588.

[66] F.H. Spedding, D.C. Henderson, High-temperature heat contents and related thermodynamic functions of seven trifluorides of the rare earths: Y, La, Pr, Nd, Gd, Ho, and Lu, J. Chem. Phys. 54 (1971) 2476–2483.

[67] S. Blundell, Magnetism in Condensed Matter, Oxford University Press Inc., New York, 2001.

[68] W. Van Den Heuvel, V.K. Tikhomirov, D. Kirilenko, N. Schildermans, L.F. Chibotaru, J. Vanacken, P. Gredin, M. Mortier, G. Van Tendeloo, V. V. Moshchalkov, Ultralow blocking temperature and breakdown of the giant spin model in Er^{3+}-doped nanoparticles, Phys. Rev. B. 82 (2010) 094421.

Highlights

- Polycrystalline samples of the orthorhombic $Yb_xY_{1-x}F_3$ solid solutions were prepared.

- The structural and microstructural properties were studied by XRD and SEM.

- The susceptibility data was analyzed within 2–300 K range.

- Complete crystal field splitting of the $^2F_{7/2}$ manifold of Yb^{3+} in YF_3 is obtained.

- $Yb_xY_{1-x}F_3$ solid solutions exhibit paramagnetic behavior.

Conflict of Interest

We wish to confirm that there are no known conflicts of interest associated with this publication and there has been no significant financial support for this work that could have influenced its outcome.

We confirm that the manuscript has been read and approved by all named authors and that there are no other persons who satisfied the criteria for authorship but are not listed. We further confirm that the order of authors listed in the manuscript has been approved by all of us.

Signed by all authors as follows:

Jelena Aleksić

Tanja Barudžija

Dragana Jugović

Miodrag Mitrić

Marko Bošković

Zvonko Jagličić

Darja Lisjak

Ljiljana Kostić